JPE 16-5-1

http://dx.doi.org/10.6113/JPE.2016.16.5.1629
ISSN(Print): 1598-2092 / ISSN(Online): 2093-4718

Bidirectional Power Conversion of Isolated Switched-Capacitor Topology for Photovoltaic Differential Power Processors

Hyun-Woo Kim*, Joung-Hu Park†, and Hee-Jong Jeon*

*,†Department of Electrical Engineering, Soongsil University, Seoul, Korea

Abstract

Differential power processing (DPP) systems are among the most effective architectures for photovoltaic (PV) power systems because they are highly efficient as a result of their distributed local maximum power point tracking ability, which allows the fractional processing of the total generated power. However, DPP systems require a high-efficiency, high step-up/down bidirectional converter with broad operating ranges and galvanic isolation. This study proposes a single, magnetic, high-efficiency, high step-up/down bidirectional DC–DC converter. The proposed converter is composed of a bidirectional flyback and a bidirectional isolated switched-capacitor cell, which are competitively cheap. The output terminals of the flyback converter and switched-capacitor cell are connected in series to obtain the voltage step-up. In the reverse power flow, the converter reciprocally operates with high efficiency across a broad operating range because it uses hard switching instead of soft switching. The proposed topology achieves a genuine on–off interleaved energy transfer at the transformer core and windings, thus providing an excellent utilization ratio. The dynamic characteristics of the converter are analyzed for the controller design. Finally, a 240 W hardware prototype is constructed to demonstrate the operation of the bidirectional converter under a current feedback control loop. To improve the efficiency of a PV system, the maximum power point tracking method is applied to the proposed converter.

Key words: Bidirectional converter, Differential power processor, Integrated inductor, Interleaved energy transfer

I. INTRODUCTION

Renewable energy resources are a promising solution to the future energy crisis and climate change. However, solar energy, one of the most promising energy sources, exhibits a fluctuating power generation profile because its generation is dependent on external environmental factors, such as temperature and radiation. A power conditioning converter is necessary in achieving a stable power generation with maximum energy efficiency. Differential power processing (DPP) converters are regarded as a novel architecture of next-generation power conditioning systems for the individual maximum power point tracking (MPPT) of multiple photovoltaic (PV) modules through a bidirectional power flow. Individual MPPT controllers for PV modules provide high MPPT efficiency even under partial shading. DPP [1] is an alternative power conversion method that passes most of PV-generated power directly to the next inverter, processing only the partially shaded mismatch to achieve local MPP with small capacity converters. Various converter topologies have been proposed for DPP architecture; examples include DPP converters, PV balancers, and PV equalizers [1]-[5]. Figure 1 shows an example of the PV-to-bus DPP architecture. A relatively high efficiency can be achieved because the converters only process the PV power necessary to compensate for the differences associated with the power generation mismatch among modules [6]. The PV-to-bus DPP architecture is considered an ideal converter architecture for distributed power sources, such as rooftop and building-integrated PV modules.

However, the high performance of DPP schemes requires the installation of distributed power converters for every PV module, as shown in the figure. Therefore, the manufacturing costs of these schemes proportionally increase with the number of PV modules. This characteristic hinders the wide use of distributed PV power systems. Converters have an

Manuscript received Dec. 2, 2015; accepted Apr. 18, 2016
Recommended for publication by Associate Editor Yan Xing.
†Corresponding Author: wait4u@ssu.ac.kr
Tel: +82-2-828-7269, Fax: +82-2-817-7961, Soongsil University
*Department of Electrical Engineering, Soongsil University, Korea

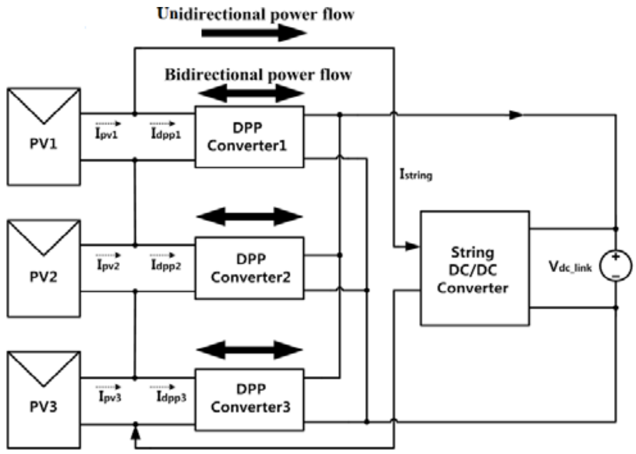

Fig. 1. Block diagram of photovoltaic (PV) power generation under differential power processing (DPP) architecture [1], [6].

intermediate connection between the individual PV modules and DC links; hence, the voltage gain should be extreme. Moreover, converters should be isolated because of the ground difference among DPP converters. Converters also require a circuit topology to achieve a high efficiency and low manufacturing cost while satisfying extreme conditions. To reduce costs for the DPP scheme, the research on topology and control parts must be coordinated efficiently. As conventional bidirectional buck-boost converters should achieve an extremely high duty cycle to obtain the input–output voltage gain, the power stresses of switches and diodes are increased significantly, followed by an increase in the switching losses caused by reverse recovery characteristics [7]-[9]. This condition results in the need for a new topology that operates under a lower voltage or current stress in comparison with existing topologies for bidirectional voltage step-up and down operations. The current work aims to find a high-efficiency, low-cost bidirectional converter topology with isolation that provides extreme voltage ratios for PV differential power processors.

Conventional research has put forward bidirectional topologies with high efficiency using soft-switching or multi-module parallel operations [10]-[16]. However, these power converters belong to non-isolated, bidirectional circuit topologies. A recent paper, which utilized zero-voltage transition and a bidirectional buck-boost topology to achieve 97% efficiency, is unsuitable for ground separation [17]. A comparative study shows current advancements in non-isolation bi-directional topologies [18]. Several high-power topologies have also been reported for isolated bidirectional applications. A combination scheme using two full-bridge converters with nine power switches has been proposed, but such scheme is unsuitable for small power applications of DPP [19]. Another bidirectional, isolated, full-bridge DC–DC converter also comprises nine power switches and two transformers, but it is too complicated for practical applications [20]. A recent achievement shows an almost optimal design comprising SiC devices for efficiency purposes, but such design require a large number of components [21].

High step-up and high efficiency requirements have also been addressed using a novel naturally clamped zero-current commutated soft-switching bidirectional current-fed full-bridge isolated DC–DC converter [22]. However, this combination scheme also comprises two full-bridge converters and eight additional power switches. Most isolated bidirectional power flow converter topologies are designed for high power applications. A recently presented bidirectional topology for multiple energy storage has one (extendable) bidirectional output, whereas another topology shows an auxiliary unidirectional output [23]. The topology remains complicated with four active switches and two magnetic devices under 10 step-up modes and 9 step-down modes satisfying the soft-switching condition, which is unsuitable for multiple-DPP architecture. Another topology for battery–DC bus applications employs a bidirectional push–pull structure with four switches and three magnetic devices under soft-switching conditions, but it only has 10 operating modes, which limit its operating range [24].

The present study proposes a simply structured bi-directional converter topology composed of a bidirectional flyback and an isolated switched-capacitor cell. In step-up mode, the output voltages of the flyback and switched-capacitor are connected in series to obtain a high gain with a high conversion efficiency even under hard-switching mode. These features broaden the operating range of the proposed topology. In step-down mode, the converter naturally undergoes an extremely low voltage step-down operation through a reciprocal operation. In addition, this converter is simple to implement under high power density with continuous energy transfer from a primary transformer to a secondary one via the ultimate interleaved operation between the flyback and switched-capacitor outputs both in the transformer core and primary and secondary copper windings. Furthermore, the converter has two operating modes under hard-switching conditions. Such characteristic contributes to a broad range of operation and simple control of bidirectional power flow. A detailed description of the operating principles and a dynamic characteristic analysis of the proposed converter topology are presented in the following sections.

II. Bidirectional Isolated Switched-Capacitor Flyback (BISCF) Converter

A. *Bidirectional Isolated Switched-Capacitor Cell*

In realizing a high step-up for the input voltage, a charge pump circuit or a switched capacitor is commonly considered. Recently, an isolated switched-capacitor circuit was

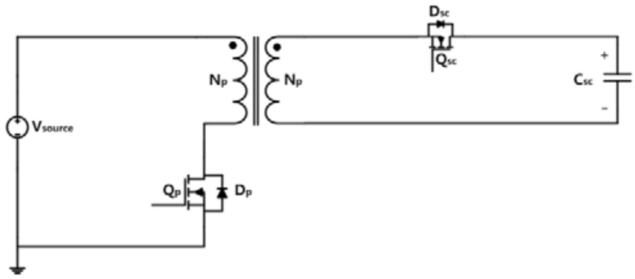

Fig. 2. Bidirectional switched-capacitor cell with isolation (note that the dot position is different from the flyback)

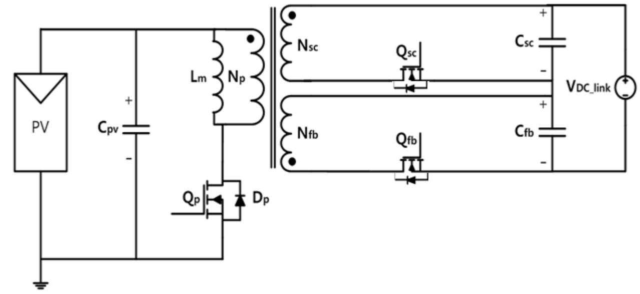

(a) Proposed bidirectional topology.

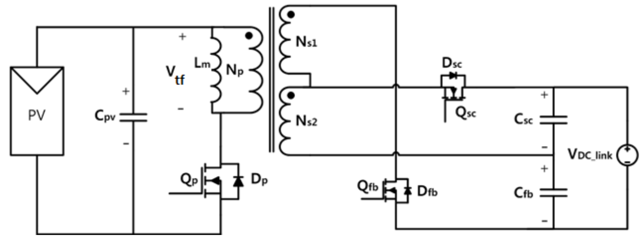

(b) Advanced version of interleaved power delivery.

Fig. 3. Equivalent circuit of the proposed (BISCF) converter.

presented in [7], but the charge–pump circuit could only operate under a unidirectional power flow and not under a bidirectional one. To rectify this disadvantage, a modified switched-capacitor circuit with a synchronous rectifier is introduced (Fig. 2). The circuit diagram is similar to that of a conventional bidirectional flyback converter. However, the dot of the transformer is on the other side, which critically determines the operation principle [7]. The circuit achieves high step-up/step-down ratios, as well as isolation capability, through the use of a high turn-ratio transformer. If the transformer is ideal, its operating performance is similar to that of conventional switched capacitors, except the voltage conversion ratios can be continuously changed according to the winding number.

B. Proposed BISCF Converter Topology

A prototype circuit of the proposed bidirectional converter is shown in Fig. 3(a). The secondary side of the transformer comprises an isolated switched capacitor and a bidirectional flyback converter employing two active switches. The cell and converter outputs are connected in series to interface with the high DC-link voltage. The proposed converters deliver the required energy to the load through the transformer core(s) whenever the main switch is turned on and off. Hence, more power is supplied to the load than any other single-ended isolation schemes at the same volume [25]-[29]. However, as secondary windings remain separate from one another, the converter is not a circuit version of a genuine interleaved power transfer. The topology is thus improved by sharing the secondary coils between the outputs of the switched capacitor and those of the flyback (Fig. 3(b)). One secondary winding N_{s2} is utilized during on and off states to improve the utilization ratio of the transformer. The details of the operating modes are described in Section II.C.

To analyze the steady-state operation of the proposed converter, we present the DC-link voltage as separate equivalent circuits (Fig. 4).

The steady-state gain of the isolated switched-capacitor cell is only related to the transformer's turn ratio such that

$$\boldsymbol{M_{VDC\_sc}} = \frac{\boldsymbol{V_{DC\_SC}}}{\boldsymbol{V_{pv}}} = \frac{\boldsymbol{N_{s2}}}{\boldsymbol{N_p}} \tag{1}$$

The steady-state gain of the flyback under continuous conduction mode is

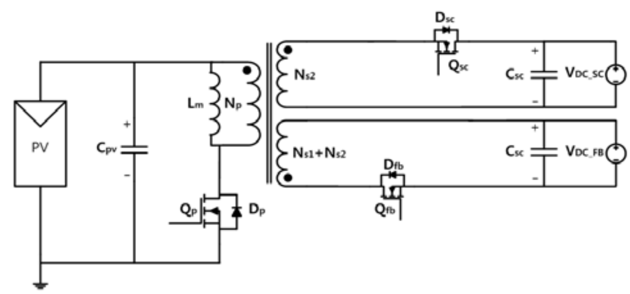

Fig. 4. Equivalent transformation of the proposed BISCF converter with separated output voltages

$$\boldsymbol{M_{VDC\_fb}} = \frac{\boldsymbol{V_{DC\_FB}}}{\boldsymbol{V_{pv}}} = \frac{\boldsymbol{D}}{\boldsymbol{(1-D)}}\frac{\boldsymbol{N_{s1}+N_{s2}}}{\boldsymbol{N_p}} \tag{2}$$

Finally, the gain of the BISCF converter under continuous conduction mode is

$$M_{VDC} = M_{VDC\_sc} + M_{VDC\_fb} = \frac{N_{s2}}{N_p} + \frac{D}{(1-D)}\frac{N_{s1}+N_{s2}}{N_p} \tag{3}$$

C. Operating Principle

The proposed converter topology under the step-up/step-down modes has two operating modes (power flow opposite for each mode), as shown in Fig. 5. Each mode has a different switching state. This simple principle contributes to the simple controller design and wide operating ranges.

Mode 1: Q_p and Q_{sc} are turned on. The path of the current conduction is shown as a solid line in Fig. 5(a). Q_{sc} operates as a synchronous rectifier with a small conduction loss and conduction path N_{s2}.

Mode 2: Q_{fb} is turned on. The path of the current conduction is shown as a solid line in Fig. 5(b). Q_{fb} operates as a synchronous rectifier with a small conduction loss and conduction path N_{s2}.

The step-down operation is exactly the same as the step-up

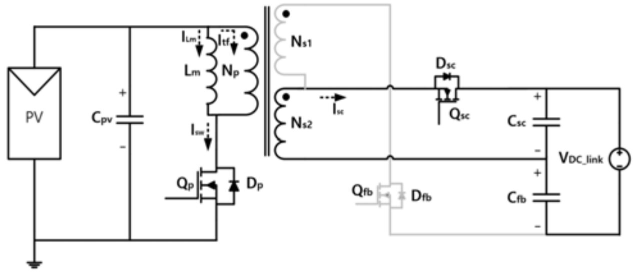

(a) Mode 1: Q_p and Q_{sc} turned on.

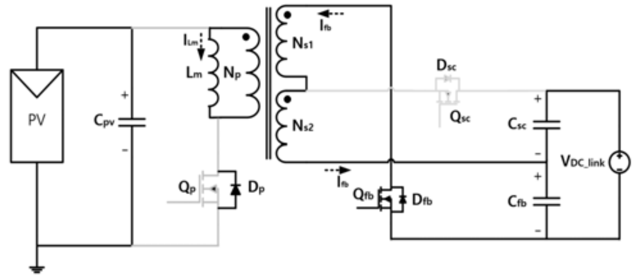

(b) Mode 2: Q_{fb} turned on as a synchronous rectifier.

Fig. 5. Equivalent circuits of each operation mode (step-up).

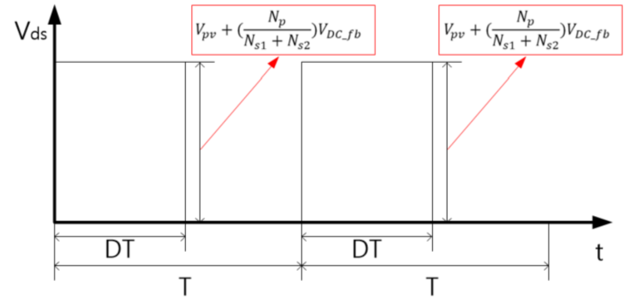

(a) Drain-source voltages of Qp.

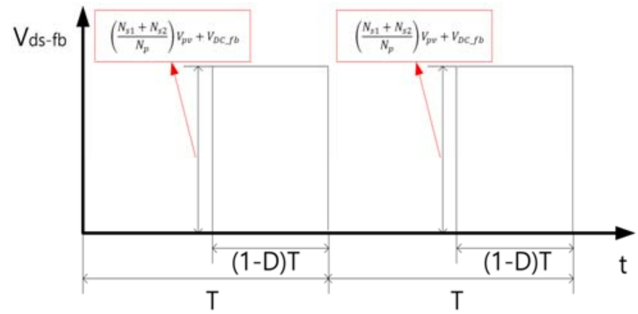

(b) Drain-source voltages of Qfb.

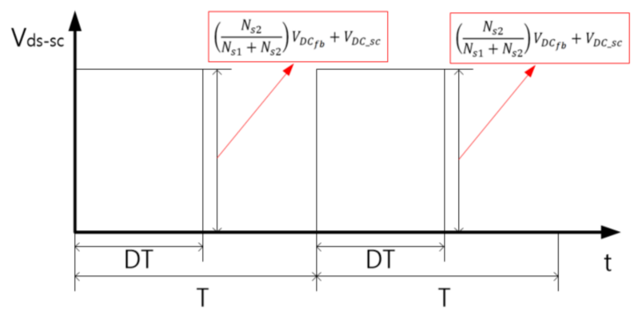

(c) Drain-source voltages of Qsc.

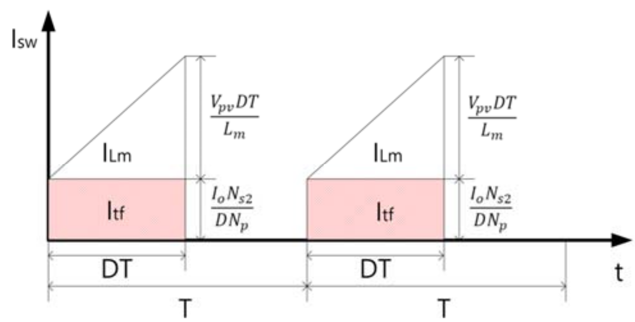

(d) Primary switch current.

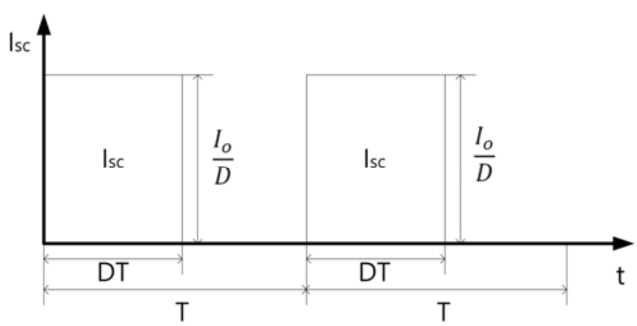

(e) Switched-capacitor switch current.

operation shown in Fig. 5, except that the direction of the average inductor current is reversed by the duty-cycle transient and the actions of the main switches and synchronous rectifiers are swapped, as in a conventional bidirectional buck-boost converter. Fig. 6 shows the pulse width modulation (PWM) operation of the switches and the detailed description of the operating principles, along with the key waveforms of the proposed converter. Fig. 7 also presents the primary and secondary switch current waveforms under the step-down mode.

D. Device Stress Analysis and Design Guidelines

This section analyzes the device stress for the proposed converter. A design example of the specification of the input and output voltage/power, such as 50 V and 400V/200 W, is shown.

The switch voltage stresses are

$$V_{pk} = V_{pv} + \left(\frac{N_p}{N_{s1}+N_{s2}}\right)V_{DC\_fb} = 90\ \text{V} \tag{4}$$

$$V_{pk-sc} = \left(\frac{N_{s2}}{N_{s1}+N_{s2}}\right)V_{DC\_fb} + V_{DC\_sc} = 360\ \text{V} \tag{5}$$

$$V_{pk-fb} = V_{pv}\left(\frac{N_{s1}+N_{s2}}{N_p}\right) + V_{DC\_fb} = 450\ \text{V} \tag{6}$$

where V_{pk}, V_{pk-sc}, and V_{pk-fb} are the respective voltage stresses of the main switch, switched capacitor, and flyback switch.

The switch current stresses are

$$I_{sw-avg} = M_{VDC}I_o = I_o\left(\frac{N_{s2}}{N_p} + \frac{D}{(1-D)}\frac{N_{s1}+N_{s2}}{N_p}\right) = 4\ \text{A} \tag{7}$$

$$I_{sc-avg} = I_o = 0.5\ A \tag{8}$$

$$I_{fb-avg} = I_o = 0.5\ A \tag{9}$$

where I_{sw-avg}, I_{sc-avg}, and I_{fb-avg} are the average current stresses for the main switch, switched capacitor, and flyback switch, respectively. The turn ratios should be considered to

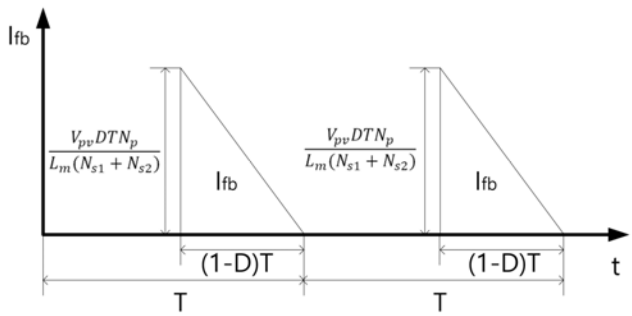

(f) Flyback switch current.

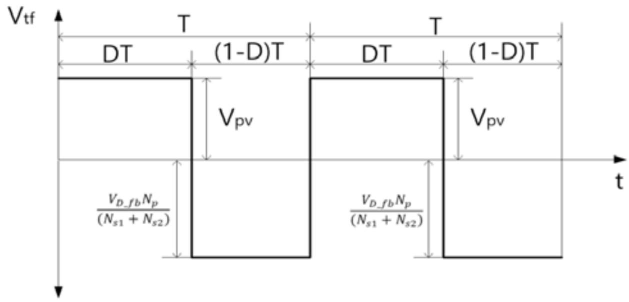

(g) Primary winding voltage.

Fig. 6. Conceptual drawings of V_{ds}, V_{ds_fb}, and V_{ds_sc} and the switch current waveforms of the proposed converter in step-up mode (drain-source voltages of Qp (V_{ds}), Qfb (V_{ds_fb}), and Qsc (V_{ds_sc})).

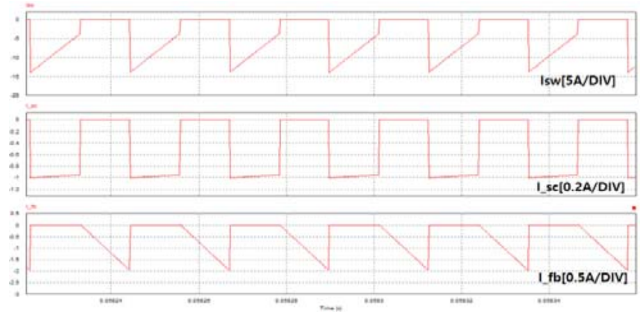

Fig. 7. Switch and transformer current/voltage waveforms of the converter under the step-down mode (drain-source currents of Qp (I_{sw}), Qfb ($I_{\_fb}$), and Qsc ($I_{\_sc}$)).

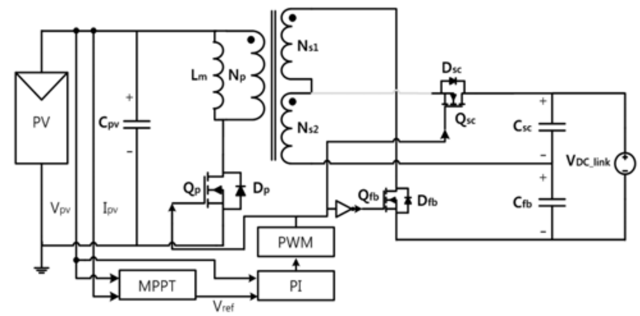

Fig. 8. Proposed converter with a PV source under MPPT control.

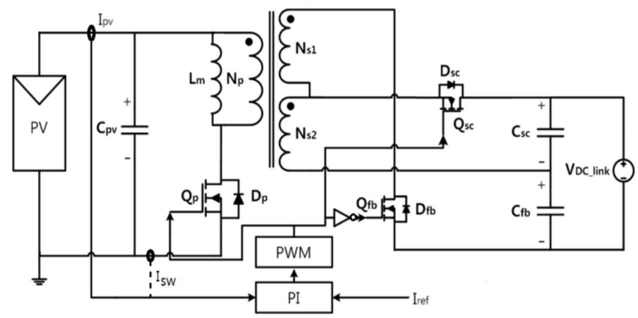

Fig. 9. Alternate controller configuration for bidirectional current flow regulation of the proposed BISFC topology.

satisfy the reasonable duty-cycle ranges, such as 0.2–0.8, under the input and output voltage variations. The analysis results show that the number of device parts for the main and secondary switches affects the stresses.

The transformer winding numbers are determined with the conventional magnetic design equation and the required turn ratios such that

$$N_p > \frac{10^4 L I_{pk}}{B_{max} A_e} = \frac{10^4 \cdot 50uH \cdot 12}{0.3(2.47)} = 8.1 \tag{10}$$

where B_{max} is the maximum allowable magnetic flux density, L is the magnetizing inductance, I_{pk} is the peak current, and A_e is the effective area of the core. The current stress of each winding is the same as that of the corresponding switch in the conduction path (Fig. 5). The present study uses a highly coupled coaxial-cabled transformer to reduce leakage inductances.

III. Dynamic Characteristic Analysis

A. Control Configuration

Fig. 8 shows the structure of the proposed non-isolated DC–DC circuit diagram of the proposed converter under MPPT control. For the perturb-and-observe algorithm in the MPPT controller, the PV voltage and current from each module are observed. The MPPT controller then updates the proportional–integral (PI) controller reference V_{ref} given to the inner loop controller. Hence, the duty cycles of the converter are generated through the inner voltage feedback loop. To show the current regulation capability of the proposed converter topology, we implement a bidirectional current control loop that is independent from the MPPT controller. Fig. 9 shows the bidirectional power flow control configuration of the proposed converter. The PI controller in a current feedback loop senses a switching current I_{pv} or I_{sw} from the primary side, produces a control voltage comparable to the reference, and then makes the duty cycle through the PWM generator. The PI controller reference I_{ref} in Fig. 9 is given by a controller that provides a step-changed bipolar signal to show the bidirectional power flow operation. The experimental results are given in Section IV.

B. Small Signal Models of the BISFC

When the controller of the proposed converter is designed for MPPT, the control-to-PV voltage transfer function must be derived. The switched-capacitor cell is considered a proportional gain in the transfer function derivation because

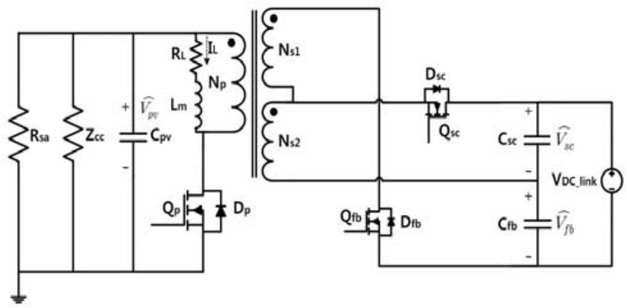

Fig. 10. Small-signal parameters for the control-to-PV voltage transfer function (Zcc is the interaction from the other PV modules).

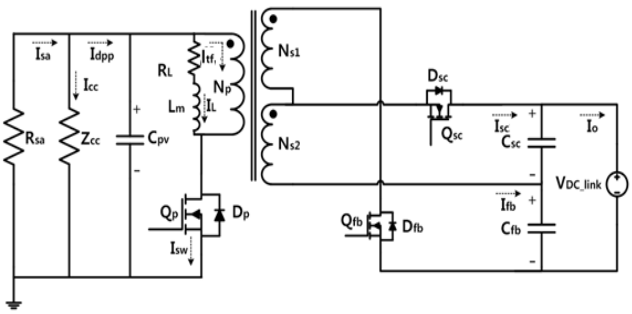

Fig. 11. Small-signal parameters for the control-to-current transfer function.

of the rapid dynamic response. The major concern is the dynamic characteristic of the flyback converter part (Fig. 10). The control-to-PV-voltage transfer function is derived as

$$\frac{\widehat{V_{pv}}}{\hat{d}}=\frac{-\left(s\frac{Z_T}{I_L}+\frac{nDV_{pv}+DV_{DC\_FB}+nZ_TR_LI_L}{nL_mC_{pv}}\right)}{s^2+s\left(\frac{Z_TR_LC_{pv}-L_m}{Z_T}\right)+\frac{Z_TD^2+nZ_TDD'-R_L}{Z_TL_mC_{pv}}}$$

$$(\mathrm{n}=N_{s1}+N_{s2}) \qquad (11)$$

where $Z_T=R_{sa}\|Z_{cc}$, R_L is the parasitic resistance of the primary winding, R_{sa} is the equivalent output resistance of the PV sources, and Z_{cc} is the equivalent input resistance of the main string converter and other modules.

When the current controller is designed for power flow regulation, the control-to-input (DPP) current I_{dpp} is derived by the state-space averaging of Fig. 11. Analysis shows that the transfer function of the control-to-DPP current is derived as follows.

From $I_{dpp}=I_{sa}-I_{cc}$, the result is

$$\frac{\widehat{I_{dpp}}}{\hat{d}}=\frac{\widehat{I_{sa}}}{\hat{d}}-\frac{\widehat{I_{cc}}}{\hat{d}}\,. \qquad (12)$$

Then, from Fig. 10,

$$\frac{\widehat{I_{dpp}}}{\hat{d}}=\frac{\widehat{V_{pv}}}{R_{sa}\hat{d}}-\frac{\widehat{V_{pv}}}{Z_{cc}\hat{d}}=\frac{\widehat{V_{pv}}}{\hat{d}}\left(\frac{1}{R_{sa}}-\frac{1}{Z_{cc}}\right) \qquad (13)$$

The final form can be derived by merging (13) with (11).

C. Simulation Results of MPPT Control and Bidirectional Power Flow

Fig. 12 shows the simulated PV voltage and current waveforms under the proposed MPPT controller. The MPP voltage is 45 V, which indicates that the controller tracks MPP well using the perturb-and-observe algorithm.

To verify the current regulation, we check the transient response of the 1A bipolar step-change in the DPP current. The switch current in Fig. 13 shows that the bidirectional power flow is regulated, as confirmed in Fig. 18.

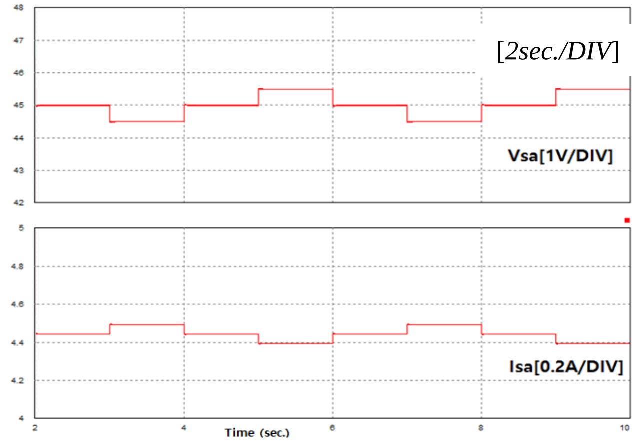

Fig. 12. MPPT control of the proposed converter in PSIM simulation (Top: PV voltage, Bottom: PV current)

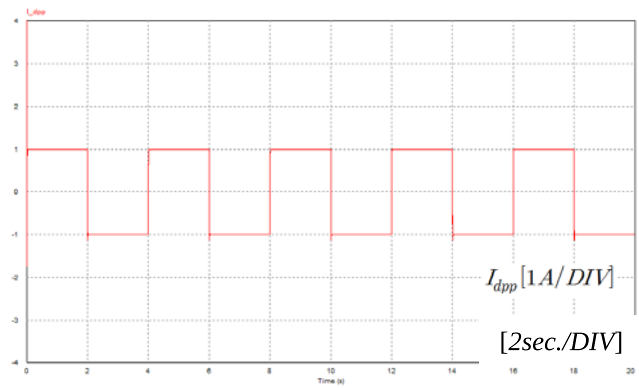

Fig. 13. Simulated 1A bipolar step-changed current (I_{dpp}) control of the proposed converter.

IV. Experimental Results

A hardware prototype of the proposed scheme was built and tested according to the design parameters in Table I. Fig. 14(a) illustrates the hardware efficiency of the proposed converter in accordance with the input voltage variation in step-up mode. The results show that the proposed converter achieves a maximum efficiency of 96%. The input voltage from 30 Vto 48 V maintains efficiency at over 94% because of the simple operating principle. Fig. 14(b) also shows the measured efficiency according to the secondary voltage variation in step-down mode. The experimental results show that the proposed converter is 96% efficient, even at the maximum voltage of 460 V. Fig. 14(c) also shows the measured efficiency according to power variation. The proposed converter is over 96.2% efficient at maximum, and

TABLE I
DIODES AND MOSFET UTILIZED IN THE CSFTI HARDWARE

Symbol	Parameter (part number)	Values
V_{pv}	PV voltage	30–48VDC
V_{dc_link}	DC-link voltage	340–460 VDC
P_{out}	Output power	240 W
f_s	Switching frequency	44 kHz
L_m	Magnetizing inductance	50 μH
Q_p	Primary switch	IRFP4568
Q_{sc}	Secondary switched capacitor cell switch	IRFP21N60L
Q_{fb}	Secondary flyback switch	IRFP21N60L
N_p: N_{s1} : N_{s2}	Turn ratio	1: 1 :4
C_{sa}	PV module capacitor	4700 μF
D_p	Primary anti-parallel diode	MBR10250
D_{fb}	Flyback anti-parallel diode	SF18
D_{sc}	Switched capacitor anti-parallel diode	SF18

the overall efficiency remains over 95% at an output of 100 W to 240 W.

The temperature distribution measurements of the hardware prototypes for topology validation are presented in Figs. 15(a) and (b). The temperature distributions of the proposed hardware show identical operating conditions, with the exception of the varying input voltage. Temperature distributions were measured with a DM-60 thermal imaging camera [30–33]. The experiment was conducted at ambient temperature, and the MOSFETs operated without any heat sinking devices. The main heat sources, such as the transformer winding (S1), core (S4), primary switch (S2), and secondary flyback switch (S3), are indicated in the figure. The temperatures of the secondary MOSFETs are not significantly different, thus indicating that the loss changes in the secondary MOSFETs are minimal despite the voltage gain. The temperature of the main switch increases from 50.4° C to 70.1° C, whereas the primary winding temperature of the transformer increases from 38.7° C to 46.4° C. The primary switch and winding loss component are dominant factors in the efficiency variation depicted in Fig. 14. Moreover, the proposed topology effectively reduces severe power stress in extreme step-up-isolated applications.

Fig. 16 shows the PWM switching waveforms of the MOSFETs in the hardware, which are consistent with the simulation results in Fig. 6. The drain-source voltages have negligible voltage spikes even without a snubber circuit because of the high coupling of the coaxial-cabled transformer. Fig. 17 shows the experimental PV voltage and current waveforms under the MPPT controller. A dual PV-array simulator was used (TerraSAS) to emulate the PV panel. Fig. 17(a) shows the V-I and V-P curves of the panel in the

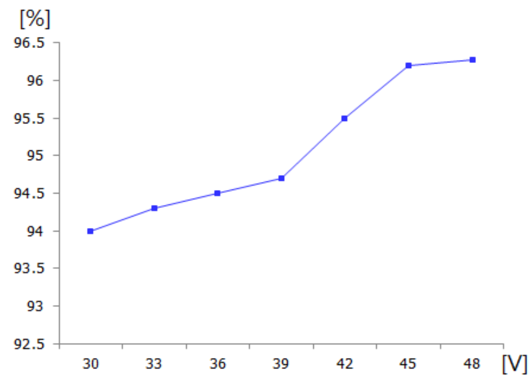

(a) Step-up mode (V_{dc_link} = 400 V, P_{out} = 200 W).

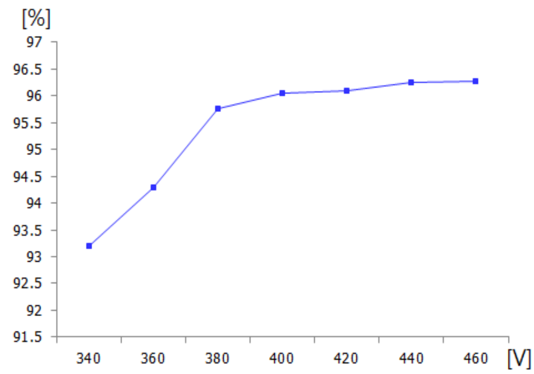

(b) Step-down mode (V_{pv} = 45 V, P_{out} = 200 W).

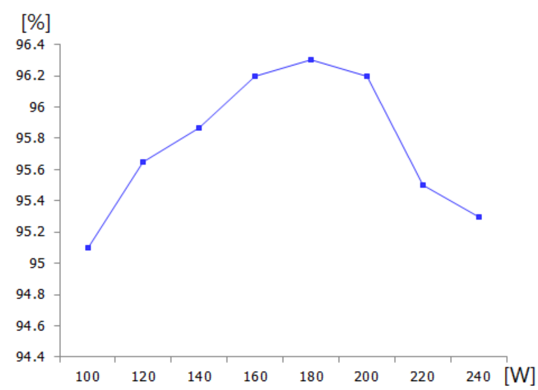

(c) Power variation (V_{pv} = 45 V, V_{dc_link} = 400 V).

Fig. 14. Prototype efficiency of the proposed converter.

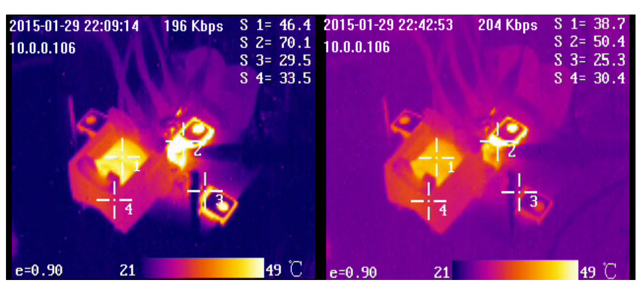

(a) V_{in} = 36 V. (b) V_{in} = 46 V.

Fig. 15. Comparison of the thermal distributions of the hardware prototypes ($V_{out} = 400V$), with the MOSFETs operating without a heat sink.

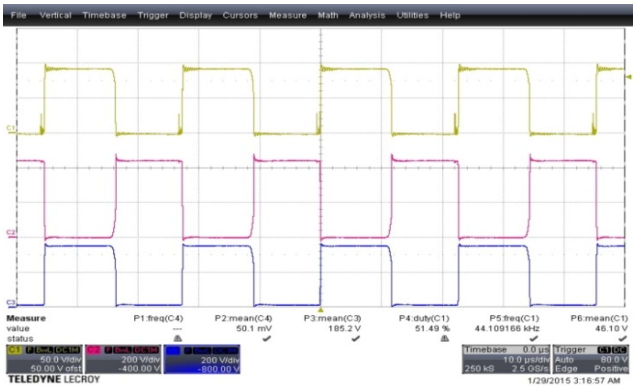

Fig. 16. V_{ds}, V_{ds_fb}, and V_{ds_sc} of the proposed converter in the hardware experiment (Channel 1: drain-source voltage of main switch [50 V/div.], Channel 2: flyback drain-source voltage [200 V/div.], Channel 3: switched-capacitor drain-source voltage [200 V/div.], time: 10 μs/div.)

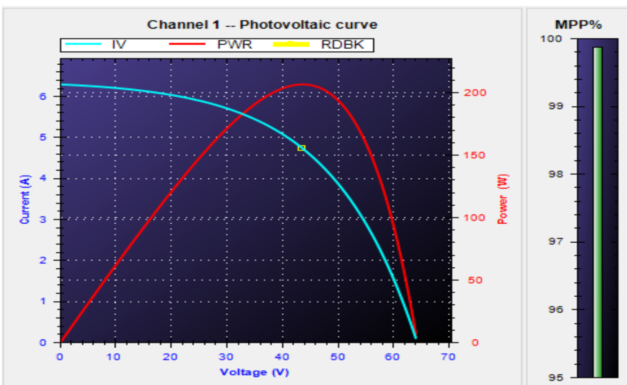

(a) V-I and V-P curves and MPPT efficiency

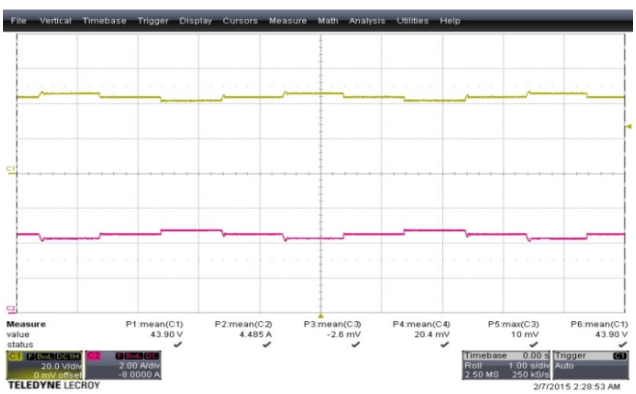

(b) PV voltage and current under MPPT control

Fig. 17. MPPT control of the proposed converter in the hardware experiment (Channel 1: solar panel voltage [20 V/div.], Channel 2: solar panel current [2 A/div.], time: 1 s/div.); the rightmost bar in the upper figure refers to the current operating MPPT efficiency.

MPPT control test. The MPP is 45 V. Thus, Fig. 17(b) shows that the controller tracks MPP well because of the PV voltage operating near the MPP.

The input current (I_{dpp}) waveform was measured with the bipolar 1A step-change of the reference to validate the bidirectional operation of the proposed topology. Fig. 18

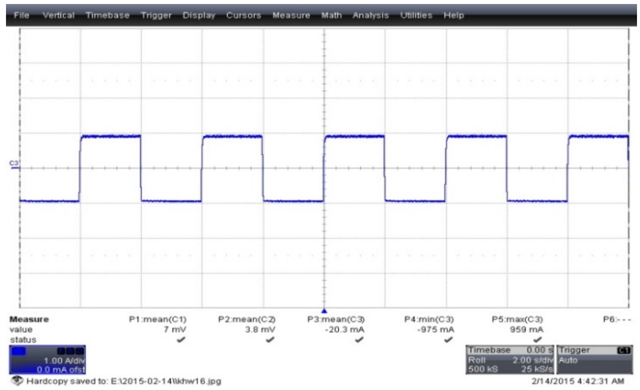

Fig. 18. DPP-input (I_{dpp}) current waveform under the current control of the proposed converter in the hardware experiment (Channel 3: differential power processor current [1 A/div.], time: 2 s/div.)

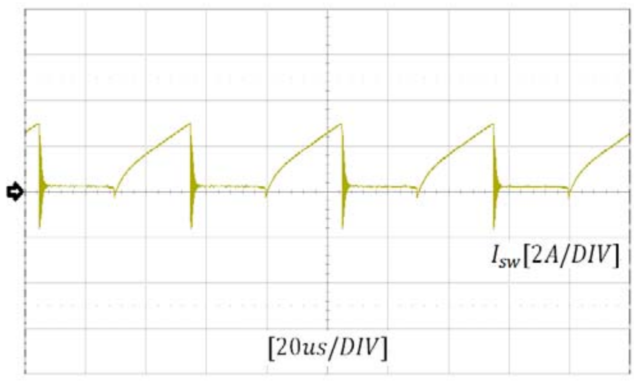

(a) Experimental primary switch current in step-up mode.

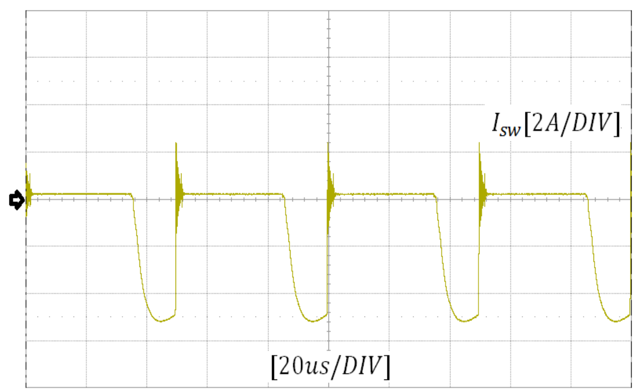

(b) Experimental primary switch current in step-down mode.

Fig. 19. Experimental switch current waveform under current control of the proposed converter.

shows that the bidirectional power flow is regulated well, even with step responses. Fig. 19 shows the switch current waveforms of the hardware prototype. Fig. 19(a) is the primary switch current in step-up mode, whereas Fig. 19(b) is the current in step-down mode. The plateau and ringing, unlike I_{sw} in Fig. 7(b), are caused by the leakage inductance of the layout and transformer resulting from the absence of snubber circuitry.

V. Conclusions

This study proposed a low-cost, high efficiency, bidirectional DC–DC power conversion circuit topology comprising of an isolated-type switched-capacitor cell and a flyback converter. The proposed topology is suitable for step-up and step-down voltage gains for DPP PV conditioning systems. Extreme step-up/step-down ratios were achieved by connecting the output terminals of the bidirectional flyback converter and the isolated bidirectional switched-capacitor converter in series. The topology structure is highly efficient, even with hard-switching action, under a broad range of operations.

The operating principle of the BISCF converter was presented with an analysis of the operating mode. Hardware experiments with a 240 W converter verified that the proposed converter could operate well in MPPT mode and bidirectional power-flow regulation mode. Moreover, the proposed converter achieves an efficiency of over 95%, even with a broad input voltage and output power variation under 400 V output operating conditions. The topology comprises only a few parts and is thus competitively affordable. The main switch should be carefully selected, as high power devices are often expensive.

Acknowledgment

This work was supported by the Human Resources Development Program (No. 20144030200600) of Korea Institute of Energy Technology Evaluation and Planning (KETEP) grant and funded by the Korea Government Ministry of Trade, Industry, and Energy.

References

[1] P. S. Shenoy, K. A. Kim, B. B. Johnson, and P. T. Krein, “Differential Power Processing for Increased Energy Production and Reliability of Photovoltaic Systems,” *IEEE Trans. Power Electron*., Vol. 28, No. 6, pp. 2968-2979, Jun. 2013.

[2] H. Zhou, J. Zhao, and Y. Han, “PV balancers: Concept, architectures, and realization,” in *Proc. IEEE Energy Convers. Congr. Expo*., pp.3749-3755, 2012.

[3] L. F. L. Villa, T.-P. Ho, J.-C. Crebier, and B. Raison, “A power electronics equalizer application for partially shaded photovoltaic modules,” *IEEE Trans. Ind. Electron*., Vol. 60, No. 3, pp. 1179-1190, Mar. 2013.

[4] S. Ben-Yaakov, A. Blumenfeld, A. Cervera, and M. Evzelman, “Design and evaluation of a modular resonant switched capacitors equalizer for PV panels,” in *Proc. IEEE Energy Convers. Congr. Expo*., pp. 4129-4136, 2012.

[5] C. Schaef, K. Kesarwani, and J. T. Stauth, “A coupled-inductormulti-level ladder converter for sub-module PV power management,” in *Proc. IEEE Appl. Power Electron. Conf*., pp. 732-737, 2013.

[6] K. A. Kim, P. S. Shenoy, and P. T. Krein, “Converter rating analysis for photovoltaic differential power processing systems,” *IEEE Trans. Power Electron*., Vol. 30, No. 4, pp. 1987-1997, Apr. 2015.

[7] D.-H. Kim, J.-H. Jang, J.-H. Park, and J.-W. Kim, “Single-ended high-efficiency step-up converter using the isolated switched-capacitor cell,” *Journal of Power Electronics*, Vol. 13, No. 5, pp. 766-778, Sep. 2013.

[8] S.-J. Park, H.-S. Lee, C.-I. Kim, J.-H. Park, H.-J. Jeon, and J. Ryeom “Controller design of a novel power conditioning system with an energy storage device for renewable energy sources under grid-connected operation,” *Journal of Power Electronics*, Vol. 13, No. 3, pp. 390-399, May 2013.

[9] S.-J. Park, J.-H. Shin, J.-H. Park and H.-J. Jeon, “Dynamic analysis and controller design for standalone operation of photovoltaic power conditioners with energy storage,” *J. Electr. Eng. Technol.,* Vol. 9, No. 6, pp. 2004-2012, Nov. 2014.

[10] Y. S. Lee and Y. Y. Chiu, “Zero-current-switched-capacitor bidirectional dc-dc converter,” *IEE Proc. Electr. Power Appl*., Vol. 152, No. 3, pp. 1525-1530, 2005.

[11] W. Yu, H. Qian, and J. S. Lai, “Design of high-efficiency bidirectional dc-dc converter and high-precision efficiency measurement,” *IEEE Trans. Power Electron*., Vol. 25, No. 3, pp.650-658, May 2010.

[12] W. Chen, P. Rong, and Z. Lu, “Snubberless bidirectional DC-DC converter with new CLLC resonant tank featuring minimized switching loss,” *IEEE Trans. Ind. Electron*., Vol. 57, No. 9, pp. 3075-3086, Sep. 2010.

[13] C.-Y. Oh, W.-Y. Sung, Y.-S. Kim, and B.-K. Lee, “Analysis of MOSFET failure modes in bi-directional phase-shift full-bridge converters,” *J. Electr. Eng. Technol.*, Vol. 10, No. 4, pp. 1692-1699, Jul. 2015.

[14] S.-H. Moon, S.-T. Jou, and K.-B. Lee, “Performance improvement of a bidirectional DC-DC converter for battery chargers using an LCLC filter,” *J. Electr. Eng. Technol.*, Vol. 10, No. 2, pp. 560-573, Mar. 2015.

[15] T.-H. Kim, J.-H. Lee, and C.-Y. Won, “Design and control methods of bidirectional DC-DC converter for the optimal DC-link voltage of PMSM drive,” *J. Electr. Eng. Technol.*, Vol. 9, No. 6, pp. 1944-1953, Nov. 2014.

[16] S. Moon, S.-G. Yoon, and J.-H. Park, “A new low-cost centralized MPPT controller system for multiply distributed photovoltaic power conditioning modules,” *IEEE Trans. Smart Grid*, Vol. 6, No. 6, pp. 2649-2658, Nov. 2015.

[17] M. R. Mohammadi and H. Farzanehfard, “Analysis of diode reverse recovery effect on the improvement of soft-switching range in zero-voltage-transition bidirectional converters,” *IEEE Trans. Ind. Electron*., Vol. 62, No. 3, pp. 1471-1479, Mar. 2015.

[18] S. Dusmez, A. Hasanzadeh, and A. Khaligh, “Comparative analysis of bidirectional three-level DC-DC converter for automotive applications,” *IEEE Trans. Ind. Electron*., Vol. 62, No. 5, pp. 3305-3315, May 2015.

[19] T. F. Wu, Y. C. Chen, J. G. Yang, and C. L. Kuo, “Isolated bidirectional full-bridge dc-dc converter with a flyback snubber,” *IEEE Trans. Power Electron*., Vol. 25, No. 7, pp. 1915-1922, Jul. 2010.

[20] T. F. Wu, J. G. Yang, C. L. Kuo, and Y. C. Wu, “Soft-switching bidirectional isolated full-bridge converter with active and passive snubbers,” *IEEE Trans. Ind. Electron*., Vol. 61, No. 3, pp.1368-1376, Mar. 2014.

[21] B. Zhao, Q. Song, W. Liu, and Y. Sun, “A synthetic discrete design methodology of high-frequency isolated bidirectional DC/DC converter for grid-connected battery energy storage system using advanced components,” *IEEE*

Trans. Ind. Electron., Vol. 61, No. 10, pp. 5402-5410, Oct. 2014.

[22] X. W. Pan and A. K. Rathore, "Novel bidirectional snubberless soft-switching naturally clamped zero current commutated current-fed dual active bridge (CFDAB) converter for fuel cell vehicles,'' *IEEE Energy Conversion Congress and Exposition*, pp. 1894-1901, 2013.

[23] R.-J. Wai and J.-J. Liaw, "High-efficiency isolated single-input multiple-output bidirectional converter," *IEEE Trans. Power Electron.*, Vol. 30, No. 9, pp. 4914-4930, Sep. 2015.

[24] T.-J. Liang and J.-H. Lee, "Novel high-conversion-ratio high-efficiency isolated bidirectional DC-DC converter," *IEEE Trans. Ind. Electron.*, Vol. 62, No. 7, pp. 4492-4503, Jul. 2015.

[25] F. Zhang and Y. Yan, "Novel forward-flyback hybrid bidirectional DC–DC converter," *IEEE Trans. Ind. Electron.*, Vol. 56, No. 5, pp. 4058–4061, May 2009.

[26] L. Huber and M. M. Jovanovi´c, "Forward-flyback converter with current-doubler rectifier: Analysis, design, and evaluation results," *IEEE Trans. Power Electron.*, Vol. 14, No. 1, pp. 184-192, Jan. 1999.

[27] Y. Kusuhara, T. Ninomiya, A. Nakayama, and S. Nakagawa, "Complete analysis of steady-state and efficiency considerations in a forward-flyback mixed converter," in *Proc. Int. Conf. Power Electron.*, pp. 620–624, 2007.

[28] J.-H. Lee, J.-H. Park, and J. H. Jeon, "Series-connected forward-flyback converter for high step-up power conversion," *IEEE Trans. Power Electron.*, Vol. 26, No. 12, pp. 3629-3641, Dec. 2011.

[29] H.-W. Kim and J.-H. Park, "Isolated bidirectional switched-capacitor flyback converter," *Electronics and Application Conference and Exposition (PEAC)*, 2014.

[30] J.-H. Park and B.-H. Cho, "Nonisolation soft-switching buck converter with tapped-inductor for wide-input extreme step-down applications," *IEEE Trans. Circuits Syst. I, Reg. Papers*, Vol. 54, No. 8, pp. 1809-1818, Aug. 2007.

[31] J.-H. Park and B. H. Cho, "The zero voltage-switching(ZVS) critical conduction mode(CRM) buck Converter with tapped-inductor," *IEEE Trans. Power Electron.*, Vol. 20, No. 4, pp. 762-774, Jul. 2005.

[32] D.-H. Kim and J.-H. Park, "High efficiency step-down flyback converter using coaxial cable coupled-inductor," *Journal of Power Electronics*, Vol. 13, No. 2, pp. 214-222, Mar. 2013.

[33] M. S. Manoharan, A. Ahmed, and J.-H. Park, "Peak-valley current mode controlled h-bridge inverter with digital slope compensation for cycle-by-cycle current regulation," *J. Electr. Eng. Technol.*, Vol.10, No.5, pp. 1989-2000, Sep. 2015.

Hyun-Woo Kim received his B.S. and M.S degrees from the Department of Electrical Engineering of Soongsil University, Seoul, Korea, in 2013 and 2015, respectively. His current research interests include the analysis of high-frequency switching converters.

Joung-Hu Park received his B.S., M.S., and Ph.D. degrees from the Department of Electrical Engineering and Computer Science of Seoul National University, Seoul, Korea, in 1999, 2001, and 2006, respectively. He was a Visiting Scholar at the Center of Power Electronics System, Virginia Polytechnic Institute and State University, Blacksburg, VA, USA, from 2004 to 2005. He is currently an Associate Professor at Soongsil University, Seoul, Korea and a Visiting Professor in the University of British Columbia, Vancouver, Canada.

Hee-Jong Jeon received his B.S. degree from Soongsil University, Seoul, Korea, his M.S. degree from Seoul National University, Seoul, Korea, and his Ph.D. degree from Chung-Ang University, Seoul, Korea, in 1975, 1977, and 1987, respectively. He was the Vice President of the Korea Institute of Power Electronics from 2000 to 2001. He is currently a Professor at Soongsil University. His current research interests include mechatronics systems, automation control, and renewable energy systems.